

Cascade of Peritectic Reactions in the B-Fe-U System

M. Dias, P.A. Carvalho, A.P. Dias, M. Bohn, N. Franco, O. Tougait, H. Noël, and A.P. Gonçalves

(Submitted September 1, 2009; in revised form November 26, 2009)

The solidification paths for UFeB_4 , UFe_3B_2 and UFe_4B , ternary compounds, situated along the $\text{U}:(\text{Fe},\text{B}) = 1:5$ line in the B-Fe-U phase diagram, are proposed based on x-ray powder diffraction measurements, differential thermal analysis, heating curves and scanning electron microscopy observations complemented with energy and wavelength dispersive x-ray spectroscopies. The compounds melt incongruently and are formed by peritectic reactions. The present work demonstrates the existence of a cascade of peritectic reactions along the $\text{U}:(\text{Fe},\text{B}) = 1:5$ composition line, establishes peritectic temperatures and proposes an isopleth diagram along this line.

Keywords microstructure, phase transformations, ternary alloy system

1. Introduction

Borides play an increasingly important role in present day engineering due to their high melting temperature as well as chemical and thermal stability. Moreover, ternary intermetallic borides of AM_xB_y type (with M a *d*-transition metal and A an actinide or rare earth) have attracted considerable interest due to a diversity of unusual physical characteristics,^[1] which extend from permanent magnetism with unusually large magnetic coercive fields, like in SmCo_4B ^[2] and SmNi_4B ,^[3] to unconventional magnetic ordering, as seen for UNi_4B .^[4]

Several compounds with atypical properties have been previously identified in U-Fe-X ternary systems (namely for $\text{X} = \text{Al}$ ^[5] or Sn ^[6]), and interesting compounds can be also expected in the B-Fe-U system. However, data on this system is scarce and requires further investigation. Results on the B-Fe-U ternary diagram were previously reported by Valyovka and Kuzma,^[7,8] who identified the UFeB_4 and UFe_3B_2 compounds. Recent systematic studies on the isothermal section at 950 °C revealed the existence of three

other ternary compounds: (i) UFe_4B , with a hexagonal structure closely related to the CeCo_4B -type structure ($a = 0.4932(1)$ nm and $c = 0.7037(2)$ nm^[9]); (ii) $\text{U}_2\text{Fe}_{21}\text{B}_6$, with a cubic Cr_{23}C_6 -type structure ($a = 1.0766(4)$ nm^[9]) and (iii) UFe_2B_6 with a CeCr_2B_6 -type structure ($a = 0.31401$ nm, $b = 0.61842$ and $c = 0.82218$ nm^[10]).

The present study aims to analyze the solidification path and identify the formation reactions of ternary compounds with an atomic $\text{U}:(\text{Fe},\text{B})$ ratio of 1:5, i.e., UFeB_4 , UFe_3B_2 and UFe_4B . This knowledge is required to establish adequate processes for pure compounds synthesis, necessary in turn to their subsequent physical properties characterization. Powder (XRD) and high temperature (HTXRD) x-ray diffraction, scanning electron microscopy (SEM), complemented with energy and wavelength dispersive x-ray spectroscopies (respectively, EDS and WDS), differential thermal analysis (DTA) and heating curves obtained from an induction furnace (IF) have been used in this study.

2. Experimental

Over 60 alloys with general $x\text{U}:y\text{Fe}:z\text{B}$ compositions were prepared by melting together the elements (purity > 99.9 at.%) in an arc furnace equipped with a cold crucible under an argon atmosphere. The surface of uranium pieces was deoxidized in diluted nitric acid prior to melting. In order to ensure homogeneity, the samples were melted at least three times before quenching to room temperature. No losses higher than 1 wt.% were observed. The high cooling rate of the solidification process enabled the solidification path of the alloys to be followed under non-equilibrium conditions. Subsequent heat treatments at 950 °C allowed inferring the transitions leading to equilibrium.

X-ray powder diffractograms of the as-cast samples were collected at room temperature with monochromatic Cu K_α radiation using an Inel CPS 120 diffractometer, equipped with a position-sensitive detector covering 120° in 2θ with a resolution of 0.03°, and a Philips X'Pert diffractometer with a 2θ -step size of 0.02° from 10 to 70°. The Powder Cell software package^[11] was used to simulate diffractograms for comparison with experimental data.

M. Dias, Departamento de Química, Instituto Tecnológico e Nuclear/CFMC-UL, P-2686-953 Sacavém, Portugal and Departamento de Engenharia de Materiais, Instituto Superior Técnico, Av Rovisco Pais, 1049-001 Lisboa, Portugal; **A.P. Gonçalves**, Departamento de Química, Instituto Tecnológico e Nuclear/CFMC-UL, P-2686-953 Sacavém, Portugal; **P.A. Carvalho**, Departamento de Engenharia de Materiais, Instituto Superior Técnico, Av Rovisco Pais, 1049-001 Lisboa, Portugal; **A.P. Dias**, Departamento de Engenharia Química e Biológica, Instituto Superior Técnico, Av. Rovisco Pais, 1049-001 Lisboa, Portugal; **M. Bohn**, Departement DRO/Geosciences Marines, Ifremer Centre de Brest, B.P. 70-29280 Plouzane, France; **N. Franco**, Departamento de Física, Instituto Tecnológico e Nuclear/CFN-UL, P-2686-953 Sacavém, Portugal; **O. Tougait** and **H. Noël**, Laboratoire de Chimie du Solide et Inorganique Moléculaire, UMR CNRS 6511, Université de Rennes 1, Avenue de Général Leclerc, 35042 Rennes, France. Contact e-mail: apg@itn.pt.

The microstructures were observed in secondary and backscattered electron modes (respectively, SE and BSE) on polished and etched surfaces using a JEOL JSM-7001F field emission gun scanning electron microscope equipped for EDS. This spectroscopy technique was primarily used for efficient x-ray map collection, whereas (quantitative) analysis was carried out with a Cameca SX100 electron microprobe micro-analyzer (EPMA) equipped with five wavelength dispersive spectrometers. In the present study, a multilayer Mo-B₄C crystal with a large interplanar distance ($2d = 210.36$ nm) was used to detect boron, a lithium fluoride (LiF) crystal ($2d = 4.03$ nm) was used to detect uranium and a pentaerythritol (PET) crystal ($2d = 8.75$ nm) was used to detect iron. The elements were analyzed simultaneously using BK α , UM β and FeK α transitions, for an acceleration voltage of 15 kV, a beam current of 20 nA, and using CeB₆, UC and α -Fe as standards. Typical beam sizes were ~ 100 nm and the interaction volume was $\sim 1 \mu\text{m}^3$. The X-phi correction software package was used to calculate the relative element proportions.^[12] Quantitative analyses were performed in 13 representative alloys with nominal compositions close to or on the U:(Fe,B) = 1:5 line. Each phase was analyzed in more than 6 randomly selected points.

DTA measurements were carried out for 6 alloys up to 1600 °C, using a Setaram DTA Labsys and employing open alumina crucibles and a permanent argon flow. Sample masses of 60-120 mg were used on the experiments. The optimized heating and cooling rates for clear peak evidence vs acquisition efficiency were 5 and 10 °C/min. The difference in temperature measured for the same transformations at different cooling rates indicated that the undercooling/overheating (ΔT) values were below 5 °C. DTA curves were normalized for mass and the transition temperatures were determined from the derivative curves. Additionally, heating curves up to 2000 °C were obtained at 10 W/min in an induction furnace (IF) coupled with an optical pyrometer. Due to the high cooling rates used to process the alloys in the arc furnace, the original microstructures were distinct from the microstructures resulting from the heating/cooling cycles. For this reason the temperatures of the transitions observed in the as-cast microstructures were essentially accessed from the heating stages of the cycles.

HTXRD was used to identify the phase transformations detected by DTA results up to 980 °C. Cu K α line was collimated with a Gobel mirror and a divergent slit of $1 \times 10 \text{ mm}^2$, and filtered with a Ge(111) two-crystal monochromator. X-ray diffractograms of as-cast U:4Fe:B samples were collected on polished surfaces with typical $11 \times 9 \text{ mm}^2$ areas. The measurements were made continuously during heating at a rate of 5 °C/min under a vacuum pressure of 10^{-4} mbar using a MBraun ASA 50M PSD detector with an acquisition time of 12 s in the 41-48° 2 θ range. The temperature was measured with a thermocouple welded to the sample surface and checked with a micro-optical pyrometer (PYRO 95). Above 700 °C, the temperature deviations detected with the pyrometer were below 1%.

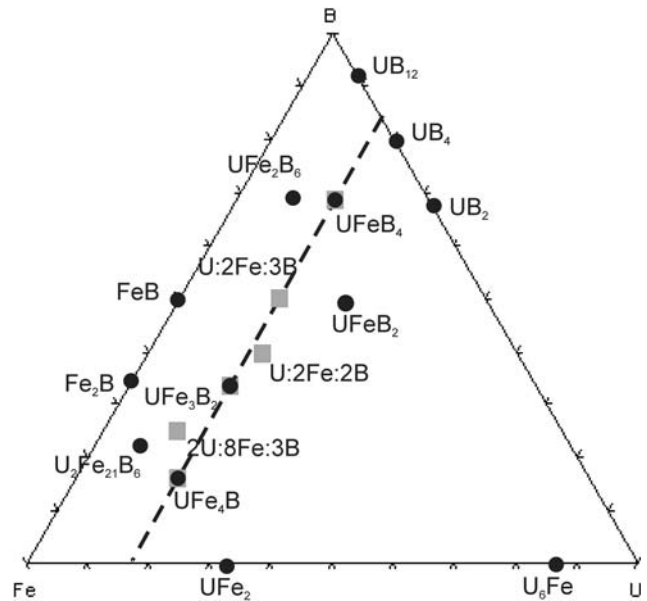


Fig. 1 Representation of binary and ternary compounds reported for the B-Fe-U system (black circles) and composition of the six alloys presented in this work (grey squares)

The results presented below are focused on the U:Fe:4B, U:2Fe:3B, U:2Fe:2B, U:3Fe:2B, 2U:8Fe:3B and U:4Fe:B alloys (Fig. 1) where the phase transformations are best evidenced.

3. Results and Discussion

Binary and ternary compounds previously identified in the B-Fe-U system are plotted as black circles in the ternary diagram shown in Fig. 1, where the composition of the representative alloys is shown as grey squares. The complex microstructures obtained for the alloys with compositions corresponding to the compounds stoichiometry, that is U:Fe:4B, U:3Fe:2B and U:4Fe:B, show they do not melt congruently.

3.1 XRD Results

Figures 2 and 3 present the XRD results obtained for the U:Fe:4B and U:3Fe:2B alloys, respectively. Although the diffractogram of the as-cast U:Fe:4B alloy evidences a significant presence of UB₄, the major peaks correspond to UFe₄B. This indicates that the UFe₄B liquidus field is close to its nominal composition. The diffractogram of the U:3Fe:2B alloy exhibits UFe₃B₂ as the predominant phase. However, UFe₄B and UFe₂ are also major phases and there is evidence of minor proportions of UFe₄B (peak at 32.5°) and α -Fe (peak at 44.7°). The U:4Fe:B alloy exhibited a diffractogram similar to the U:3Fe:2B one, evidencing however a less significant presence of UFe₄B and a slight increase of UFe₄B and α -Fe.

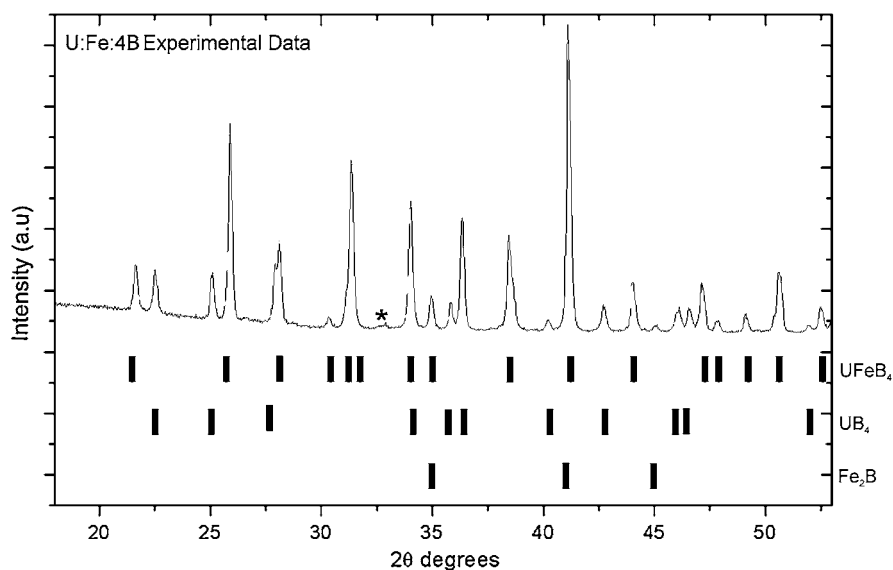


Fig. 2 Experimental x-ray diffractogram of the U:Fe:4B alloy with indication of peak localization for the phases present (UFeB_4 , UB_4 and Fe_2B compounds). The U:Fe:4B alloy presents major peaks of UFeB_4 and minor peaks of UB_4 and Fe_2B . The star indicates an incipient peak of UB_2

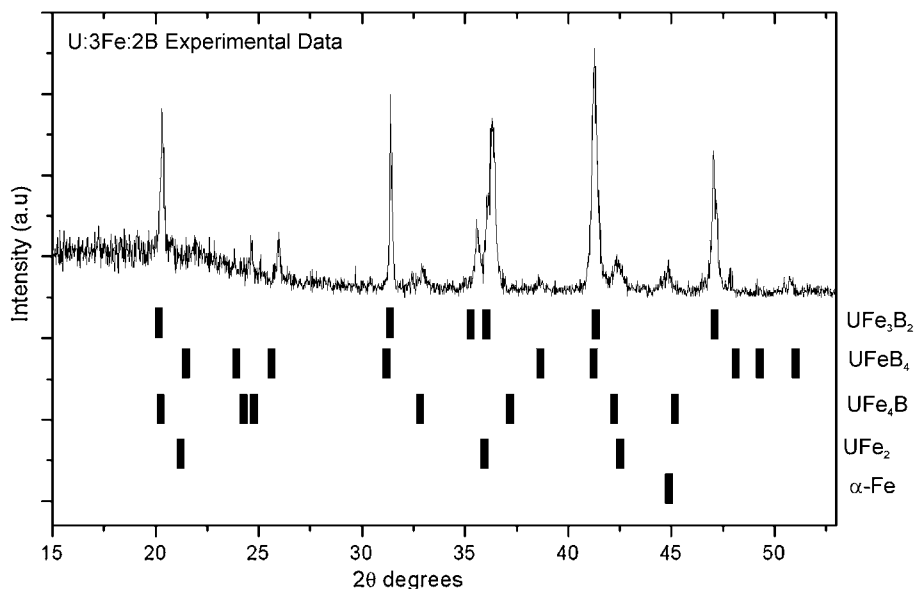


Fig. 3 Experimental x-ray diffractogram of the U:3Fe:2B alloy with indication of peak localization for the phases present (UFe_3B_2 , UFeB_4 , UFe_2 , UFe_4B , compounds and $\alpha\text{-Fe}$). The alloy presents major peaks of UFe_3B_2 , overlapping with UFeB_4 ones, and minor peaks of UFe_4B , UFe_2 and $\alpha\text{-Fe}$

3.2 Microstructural Characterization

Typical microstructures of alloys with nominal composition corresponding to the compounds stoichiometry are presented in Fig. 4. The phase labeling, average composition (AV) and composition standard deviation (SD) are presented in Table 1.

According to the SEM images, the U:Fe:4B as-cast microstructure presents three differentiated regions,

designated as A, B and G (Fig. 4a1 and a2), which, in agreement with the EPMA and EDS results (Table 1), correspond to UB_4 , UFeB_4 and Fe_2B respectively. The dendritic morphology of UB_4 (bright phase in Fig. 4a1), indicates that crystallization started with this phase. The UB_4 dendrites evidence surrounding of UFeB_4 phase (see Fig. 4a) and suggest a partial replacement during the subsequent solidification by a peritectic reaction, which implies a

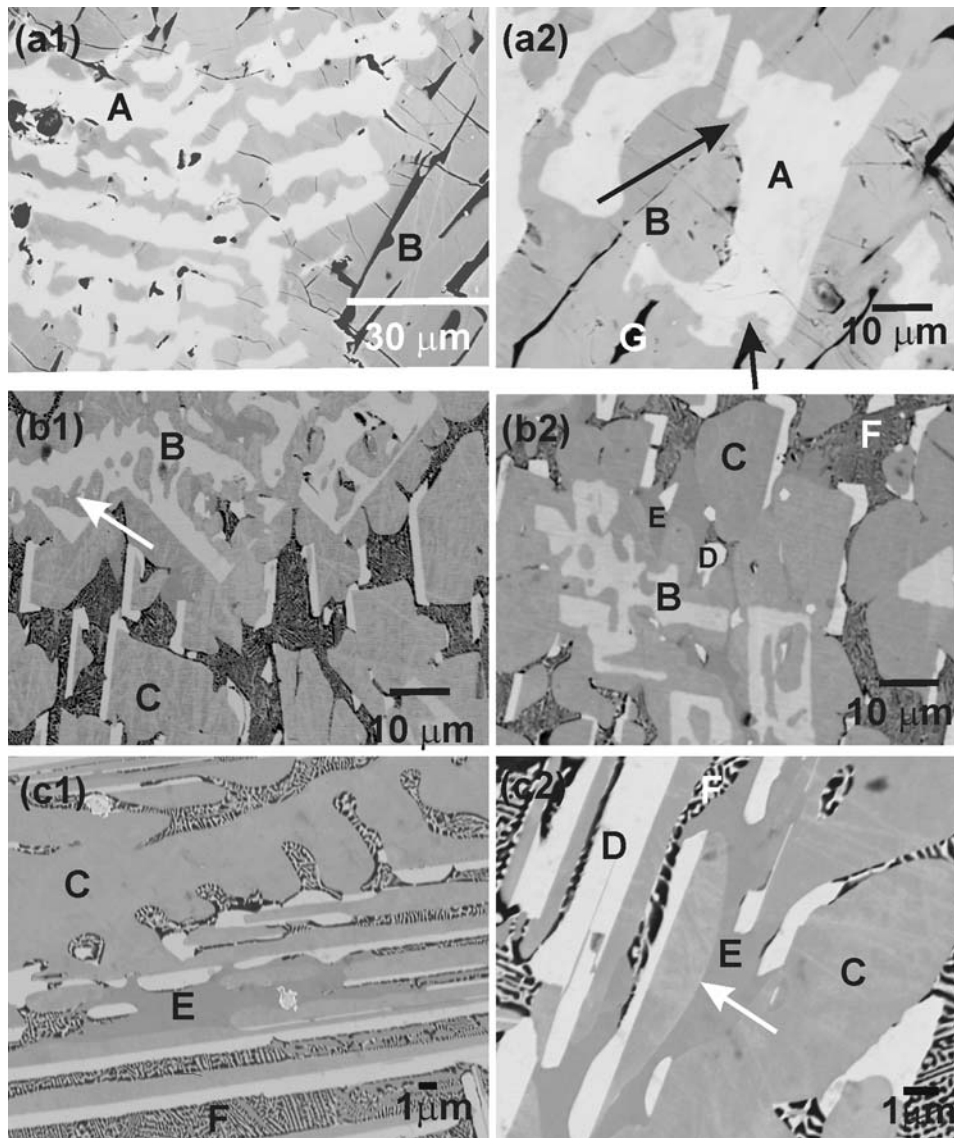


Fig. 4 BSE images representing the typical microstructure at different scales of U:Fe:4B (a1 and a2), U:3Fe:2B (b1 and b2) and U:4Fe:B (c1 and c2) alloys. The phase labelling is given in Table 1. The arrows point to phase consumption in peritectic reactions

Table 1 Region labeling, electron-probe microanalysis results and corresponding phase(s)

Label	U, at.%		Fe, at.%		B, at.%		Elemental proportion	Phase(s)
	AV	SD	AV	SD	AV	SD		
A	UB ₄
B	15.37	0.10	16.57	0.22	68.05	0.30	U _{1.00} Fe _{1.07(8)} B _{4.42(6)}	UFeB ₄
C	15.96	0.09	50.18	0.24	33.85	0.21	U _{1.00} Fe _{3.14(4)} B _{2.12(0)}	UF ₃ B ₂
D	33.81	0.33	66.76	1.03	0.00	0.00	U _{1.00} Fe _{1.97(4)}	UF ₂
E	13.28	0.23	71.46	0.51	15.26	0.66	U _{1.00} Fe _{5.37(9)} B _{1.14(8)}	UF ₄ B
F	UF ₄ B + UF ₂ + α-Fe
G	Fe ₂ B
H	UF ₃ B ₂ + UF ₂
I	UF ₂ + Fe

Section I: Basic and Applied Research

boundary reaction between the UB_4 and $UFeB_4$ liquid fields of the type:



The microstructure of the U:3Fe:2B alloy, shown in Fig. 4 (b1) and (b2), presents a bright dendritic phase of primary crystallization (region B), a surrounding darker phase (region C), bright plates (region D), elongated patches of a darker E phase surrounding regions C and D, and an interdendritic ternary eutectic (region F). EPMA results indicate that phases B, C, D, and E correspond respectively to $UFeB_4$, UFe_3B_2 , UFe_2 and $UFeB_4$ (Table 1). The dendrite morphology of $UFeB_4$ phase suggest that this phase was partly consumed in a peritectic reaction during the subsequent solidification of UFe_3B_2 , implying a boundary reaction between the $UFeB_4$ and UFe_3B_2 liquid fields of the type:



Solidification was followed by formation of UFe_4B through an also apparent peritectic reaction, which implies a boundary reaction between the UFe_3B_2 and UFe_4B liquid fields of the type:

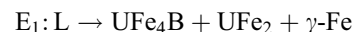


with an ensuing crystallization of UFe_2 (regions D). The crystallization of this binary congruent compound from the

ternary composition liquid implies a boundary reaction between the UFe_3B_2 and UFe_2 liquidus fields of the type:



and solidification ended at the ternary eutectic reaction (region F):



The microstructure of the U:4Fe:B alloy, shown in Fig. 4(c1) and (c2) is similar to the previous one, with the absence of L_1 reaction product and increased evidence of reactions L_3 , L_4 and E_1 , in agreement with the XRD results. The consumption of UFe_3B_2 during formation of the peritectic UFe_4B is suggested from the examination of Fig. 4(c1) and (c2).

A close inspection of the alloys microstructures confirmed the eutectic nature of L_4 and E_1 reactions. As shown in Fig. 5(a), in alloys with $U:(Fe,B) > 1:5$, such as U:2Fe:2B, the L_4 reaction produces a lamellar binary mixture of UFe_3B_2 and UFe_2 . As shown in Fig. 5(b), region F is a ternary eutectic constituted by an Fe-rich phase (dark in BSE imaging and which according to the XRD results is $\gamma\text{-Fe}$), UFe_4B (these eutectic lamellas stem from the surrounding UFe_4B patches with similar contrast) and UFe_2 (these bright eutectic lamellas stem from the surrounding UFe_2 plates with similar contrast).

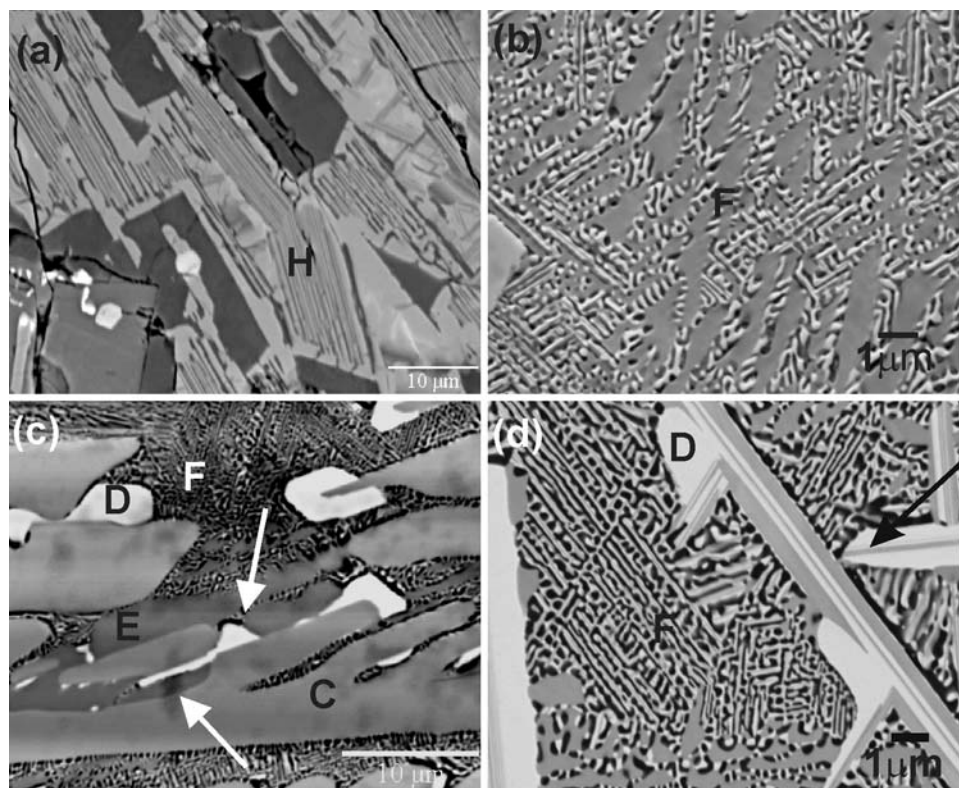
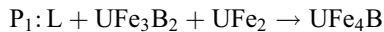


Fig. 5 (a) Eutectic reaction L_4 (region H) in the U:2Fe:2B alloy. (b) Ternary eutectic (E_1) in the U:2Fe:3B alloy. (c) Consumption of both UFe_3B_2 and UFe_2 in association with UFe_4B formation (P_1) in the 2U:8Fe:3B alloy. The arrows point to consumed recesses of regions C and D. (d) Lamellar $UFe_4B + UFe_2$ eutectic mixture (L_5) in the U:4Fe:B alloy

Figure 4(b2) and (c2) evidence a competition between reactions L_3 and L_4 , i.e., while the U:3Fe:2B microstructure in (b2) shows that UF_4B formed around UF_3B_2 before and competing with UF_2 ; the U:4Fe:B microstructure in (c2) shows that UF_2 is formed around UF_3B_2 before UF_4B . These results indicate that L_3 and L_4 converge at or near the U/(Fe,B) = 1:5 line, where the two alloys lie. The detected general prevalence of L_4 over L_3 can be justified by the fact that local composition variations tend to induce a liquid composition slide down towards the L_4 eutectic valley. On the other hand, some microstructures revealed that formation of UF_4B (region E) involved consumption of both UF_3B_2 (C) and UF_2 (D) (Fig. 5c). Therefore, the phase transformation at the L_3 and L_4 convergence point corresponds to a ternary peritectic reaction of the type:



The transition between the invariant reactions, P_1 and E_1 , occurs through the formation of a lamellar binary eutectic (evidenced in Fig. 5d), implying:



The solidification sequence presented above establishes a cascade of peritectic reactions along the U:(Fe,B) = 1:5 line:

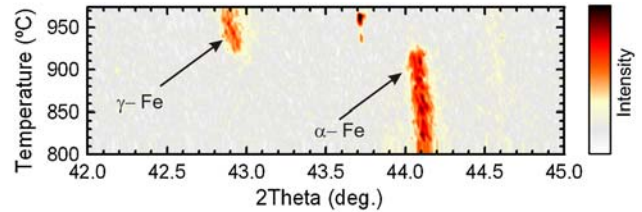


Fig. 6 HTXRD results of α -Fe to γ -Fe transformation

Table 2 Temperatures extracted from the DTA signals and IF results and relation with the transformations inferred from the microstructures

Sample composition	Reactions	Temperature, °C	Technique
U:4Fe:B	• Allotropic transformation α -Fe \rightarrow γ -Fe	940	DTA
	• Ternary eutectic (E_1) $UF_4B + UF_2 + \gamma$ -Fe \rightarrow L	980	DTA
	• Boundary reaction (L_5) $UF_4B + UF_2 \rightarrow$ L	1020	DTA
	• Ternary peritectic (P_1) $UF_4B \rightarrow$ L + $UF_3B_2 + UF_2$	1100-1170	DTA
	• Boundary reaction (L_4) $UF_3B_2 + UF_2 \rightarrow$ L		
U:3Fe:2B	• Ternary eutectic (E_1) $UF_4B + UF_2 + \gamma$ -Fe \rightarrow L	980	DTA
	• Boundary reaction (L_3) $UF_4B + UF_2 \rightarrow$ L	1210	DTA
	• Boundary reaction (L_4) $UF_3B_2 + UF_2 \rightarrow$ L		
	• Melting of UF_3B_2 $UF_3B_2 \rightarrow$ L	1250	DTA
U:2Fe:3B	• Ternary eutectic (E_1) $UF_4B + UF_2 + \gamma$ -Fe \rightarrow L	980	DTA
	• Boundary reaction (L_3) $UF_4B + UF_2 \rightarrow$ L	1200	DTA
	• Boundary reaction (L_4) $UF_3B_2 + UF_2 \rightarrow$ L		
	• Boundary reaction (L_3) $UF_4B \rightarrow$ L + UF_3B_2	1200	DTA
2U:8Fe:3B	• Ternary eutectic (E_1) $UF_4B + UF_2 + \gamma$ -Fe \rightarrow L	980	IF/DTA
	• Melting of UF_3B_2 $UF_3B_2 \rightarrow$ L	1240	IF/DTA
	• Boundary reaction (L_2) $UF_3B_2 \rightarrow$ L + UF_4B	1650	IF
	• Boundary reaction (L_1) $UF_4B \rightarrow$ L + UB_4	1880	IF

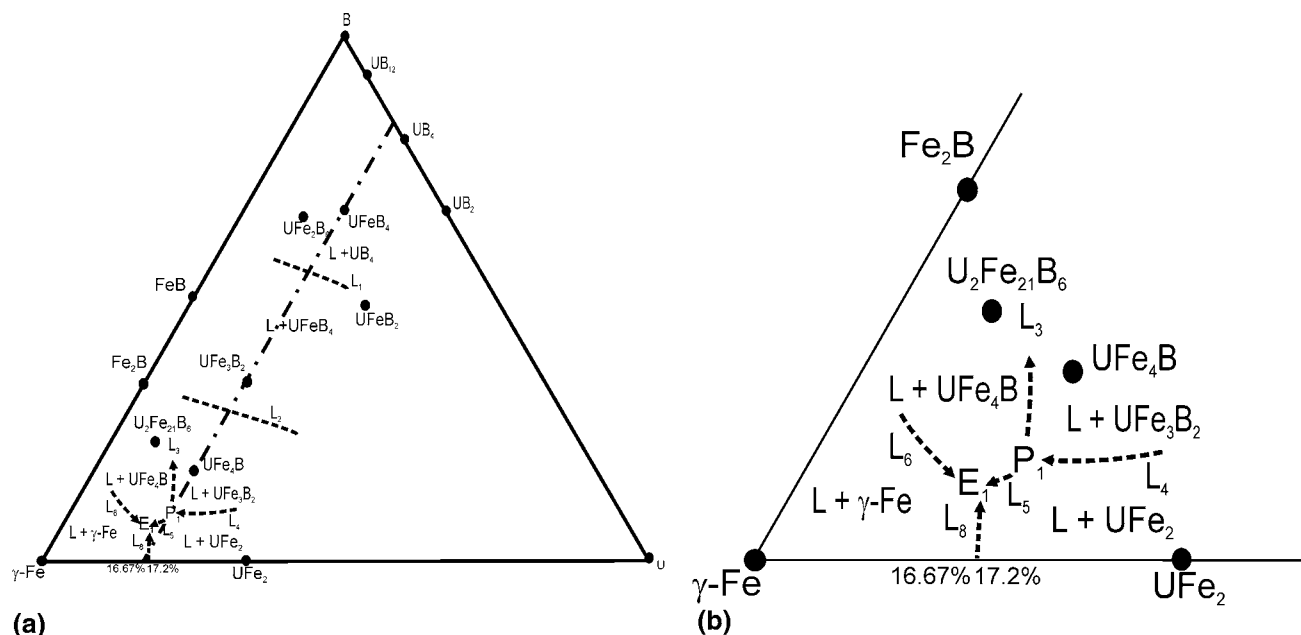
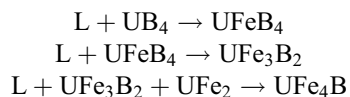


Fig. 7 (a) Liquidus projection across the U:(Fe.B) = 1:5 vertical section. (b) Magnified detail



showing that the formation temperature of the compounds decreases in the above order.

3.3 Transition Temperatures

Several exothermic transitions were detected with DTA by heating the as-cast alloys up to 1600 °C (Table 2). Heating curves obtained from an induction furnace equipped with an optical pyrometer revealed the same type of transformations up to 1600 °C and two additional thermal signals between 1600 °C and 2000 °C (also in Table 2). These results were interpreted on the basis of the microstructural constituents observed in the as-cast microstructure prior to heating: the lowest transformation temperature corresponds to the α -Fe \rightarrow γ -Fe allotropic transition (not always detected in the curves). This result was confirmed by HTXRD as can be observed in Fig. 6, where the peak corresponding to α -Fe disappears at 930-940 °C and is replaced by the peak corresponding to γ -Fe. Martensite plates have been detected inside α -Fe dendrites in the post-mortem microstructure, indicating boron supersaturation. Solute diffusion and the lack of grain boundaries (especially triple joints^[13]) are expected to have induced the large overheating detected for the 912 °C allotropic α -Fe to γ -Fe transformation.

Considering the solidification paths described above, the next signal originates from the ternary eutectic (E_1) melting, followed by melting of the UFe_4B and UFe_2 eutectic mixture (not always detected in the curves), by the melting and peritectic decomposition of the UFe_4B compound (frequently associated with melting of L_3 and L_4 products,

since these reactions converge at the ternary peritectic point), and, at higher temperatures, by the melting and peritectic decomposition of UFe_3B_2 , and by the melting and peritectic decomposition of $UFeB_4$.

3.4 Liquidus Projection and Isoleth at U:(Fe.B) = 1:5 (16.67 at.% U)

The high cooling rate used to process the as-cast alloys hindered diffusion in the solid state and allowed the inference of a liquid path across the ternary diagram from the post-mortem microstructures. Based on the experimental results, a liquidus projection across the U:(Fe.B) = 1:5 line is proposed in Fig. 7. Alloys with 1:5 proportion presenting primary solidification above L_1 (both in B content and temperature) show a deviation of the liquid composition to the left due to UB_4 crystallization. As a result, these alloys exhibit phases situated on the left of the 1:5 line, such as Fe_2B (region G in Fig. 4a and b). On the other hand, in alloys with 1:5 proportion presenting primary crystallization below L_1 (through either $UFeB_4$ or UFe_3B_2 crystallization) the liquid composition is bound to follow the line (besides local composition variations), only to be departed when the congruent binary compound UFe_2 forms after point P_1 . After this point the liquid follows the L_5 eutectic valley and solidification ends at the E_1 ternary eutectic, positioned to the left of the 1:5 line.

The vertical section at 16.67 at.% U is given in Fig. 8. The isopleth through 16.67 at.% U intercepts two-four-phase reaction planes at 1100 °C ($L + UFe_3B_2 + UFe_2 \rightarrow UFe_4B$) and 980 °C, ($L \rightarrow UFe_2 + UFe_4B + \gamma$ -Fe). The isopleth position in the quaternary planes is defined in Fig. 9. The isopleth section crosses also four-three phase reaction lines L_1 , L_2 and L_8 (the intersections are indicated

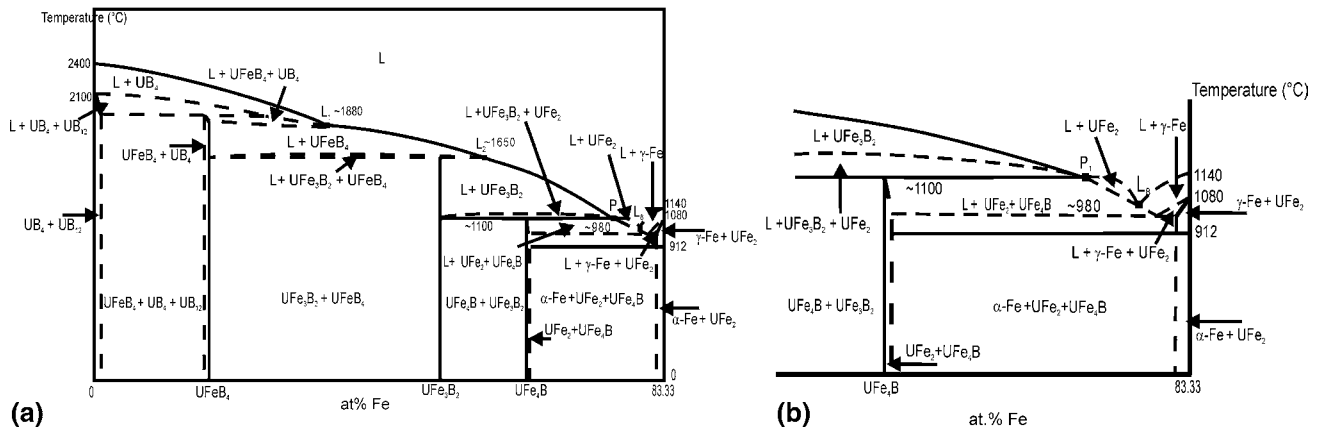


Fig. 8 (a) Isopleth at 16.67 at.% U. The squares indicate intersections with boundary reactions in the liquidus projection. (b) Magnified detail of the 16.67 at.% U isopleth proposed for the iron-rich corner. The lines position is approximate

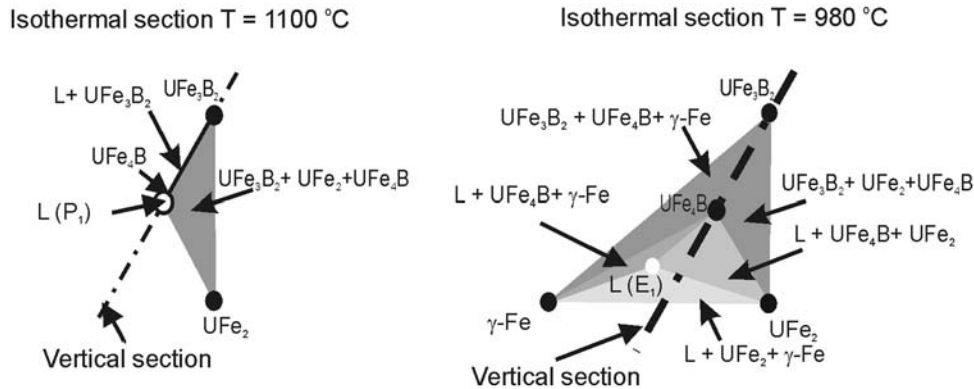
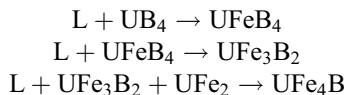


Fig. 9 Four-phase reaction planes at 1100 °C (P₁) and at 980 °C (E₁)

by squares) in agreement with the liquidus projection in Fig. 7, where L₈ represents the boundary reaction L → γ-Fe + UFe₂ originating in the Fe-U binary diagram.

4. Conclusions

Powder x-ray diffraction analysis, SEM observations complemented with EDS, DTA and heating curves of as-cast alloys demonstrated that the UFeB₄, UFe₃B₂ and UFe₄B compounds lying on the U:(Fe,B) = 1:5 line of the B-Fe-U system are formed by peritectic reactions. This justifies the complex microstructures and the presence of primary crystallization phases other than the expected compound for the stoichiometric compositions. A cascade of peritectic reactions was found to exist along the U:(Fe,B) = 1:5 line:



Therefore the solidification paths show that the formation temperatures of the compounds decrease in the above order. Solidification ends with the ternary eutectic of UFe₂ + UFe₄B + γ-Fe at 980 °C. The isopleth diagram at 16.67 at.% U proposed represents fundamental knowledge for the synthesis of pure compounds, necessary for physical properties characterization.

Acknowledgments

This work was partially supported by the exchange Program FCT/CMRS 2009-2010 and FCT, Portugal, under the contract no. PTDC/QUI/65369/2006.

References

1. P. Rogl, Ternary and Higher Order System of the Actinides and Boron, *Handbook on the Physics and Chemistry of the Actinides*, Vol 6, A.J. Freeman and C. Keller, Ed., Elsevier Science BV, 1991, p 75

Section I: Basic and Applied Research

2. H. Ido, K. Konno, H. Ogata, K. Sugiyama, H. Hachino, M. Date, and K. Maki, Magnetic Study of SmCo_5 , PrCo_5 , SmCo_4B and $\text{Sm}_3\text{Co}_{11}\text{B}_4$ Under Pulse High Field, *J. Appl. Phys.*, 1991, **70**, p 6128-6130
3. C. Mazundar, R. Nagarajan, L.C. Gupta, B.D. Padalia, and R. Vijayarahavan, SmNi_4B : A Narrow Domain-Wall Ferromagnet, *Appl. Phys. Lett.*, 2000, **6**, p 895
4. S.A.M. Mentik, A. Drost, G.J. Nieuwenhuys, A.A. Menovsky, and J.A. Midosh, Anisotropic f-electron Magnetism in UNi_4B , *Phys. B Phys. Condens. Matter*, 1994, **194**, p 275-276
5. A.P. Gonçalves and H. Noël, Isothermal Section at 850 °C of the U-Fe-Al Ternary System, *Intermetallics*, 2004, **13**, p 580-585
6. H. Noël and A.P. Gonçalves, Isothermal Section at 750°C of the U-Fe-Sn Ternary System, *Intermetallics*, 2001, **9**, p 473-479
7. I.P. Valyovka and Yu.B. Kuzma, New Uranium Borides with the Structure of YCrB_4 Type, *Dopov. Akad. Nauk Ukr. RSR, A: Fiz.-Tekhn. Mat. Nauki*, 1975, p 652
8. I.P. Valyovka and Yu.B. Kuzma, New Ternary Borides with Structures of CeCo_3B_2 and CeCo_4B Type, *Dopov. Akad. Nauk Ukr. RSR, A: Fiz.-Tekhn. Mat. Nauki*, 1974, p 1029
9. M. Dias, P.A. Carvalho, O. Sologub, O. Tougait, H. Noël, C. Godart, E. Leroy, and A.P. Gonçalves, Isothermal Section at 950°C of the U-Fe-B Ternary System, *Intermetallics*, 2007, **15**, p 413-418
10. M. Dias, P.A. Carvalho, O. Sologub, and A.P. Gonçalves, Crystal Structure of UFe_2B_6 and UFeB_2 Compounds, *Intermetallics* (to be submitted to publication)
11. G. Nozle and W. Kraus, *Powder Cell for Windows, Version 2.2*, Federal Institute for Materials Research and Testing, Berlin, 1999
12. C. Merlet, An Accurate Computer Correction Program for Quantitative Electron Probe Microanalysis, *Microchim. Acta*, 1994, **114/115**, p 363-376
13. R. Angers and A. Couture, The Alpha Gamma Transformation Mechanisms in Iron Particles, *Metall. Trans. A*, 1987, **18**, p 1151-1153